Science Bulletin

Hidden spin polarization in the 1*T*-phase layered transition-metal dichalcogenides MX_2 (*M* = Zr, Hf; *X* = S, Se, Te)

Cheng Cai, Sun Jia-Tao, Chen Xiang-Rong and Meng Sheng

Citation: Science Bulletin **63**, 85 (2018); doi: 10.1016/j.scib.2017.12.003

View online: http://engine.scichina.com/doi/10.1016/j.scib.2017.12.003

View Table of Contents:http://engine.scichina.com/publisher/scp/journal/SB/63/2

Published by the Science China Press

Science Bulletin 63 (2018) 85–91

Contents lists available at ScienceDirect

Science Bulletin

journal homepage: www.elsevier.com/locate/scib

Science Bulletin
www.scibull.com

Article

Hidden spin polarization in the 1*T*-phase layered transition-metal dichalcogenides MX_2 (*M* = Zr, Hf; *X* = S, Se, Te)

Cai Cheng [a,b], Jia-Tao Sun [b], Xiang-Rong Chen [a,*], Sheng Meng [b,*]

[a] Institute of Atomic and Molecular Physics, College of Physical Science and Technology, Sichuan University, Chengdu 610064, China
[b] Institute of Physics, Chinese Academy of Sciences, Beijing 100190, China

ARTICLE INFO

Article history:
Received 3 September 2017
Received in revised form 24 October 2017
Accepted 30 November 2017
Available online 6 December 2017

Keywords:
Hidden spin polarization
Transition-metal dichalcogenides
1*T*-phase
Helical spin texture
Centrosymmetric

ABSTRACT

The recent discovery of hidden spin polarization emerging in layered materials of specific nonmagnetic crystal is a fascinating phenomenon, though hardly explored yet. Here, we have studied hidden spin textures in layered nonmagnetic 1*T*-phase transition-metal dichalcogenides MX_2 (*M* = Zr, Hf; *X* = S, Se, Te) by using first-principles calculations. Spin-layer locking effect, namely, energy-degenerate opposite spins spatially separated in the top and bottom layer respectively, has been identified. In particular, the hidden spin polarization of β-band can be easily probed, which is strongly affected by the strength of spin–orbit coupling. The hidden spin polarization of ξ-band locating at high symmetry M point (conduction band minimum) has a strong anisotropy. In the bilayer, the hidden spin polarization is preserved at the upmost Se layer, while being suppressed if the $ZrSe_2$ layer is taken as the symmetry partner. Our results on hidden spin polarization in 1*T*-phase dichalcogenides, verifiable by spin-resolved and angle-resolved photoemission spectroscopy (ARPES), enrich our understanding of spin physics and provide important clues to search for specific spin polarization in two dimensional materials for spintronic and quantum information applications.

1. Introduction

Layered transition-metal dichalcogenides (TMD) in the form of MX_2 (*M* = Metal, *X* = S, Se, Te) have attracted intensive attentions thanks to the fact that they serve as a playground for diverse fundamental phenomena and potential applications [1–11]. Depending on how the chalcogenide atoms are sitting on each side of the metal layer, there are two polymorphs for monolayer TMDs: 1*T*-phase with D_{3d} point group and 2*H*-phase with D_{3h} point group. The physical properties of molybdenum disulfide (MoS_2) with the 2*H* structure, as a representative two-dimensional (2D) TMDs, have been widely studied. It exhibits a series of intriguing attributes that are different from its bulk form, including switchable thickness-dependent band gap [12], strong photoluminescence [13], special magnetic structure by transition metal doping [14–16], and nonlinear Rashba spin splitting under external electric field [17]. Compared with 2*H* TMDs, 1*T*-phase TMDs receive relatively less attention, but might also possess outstanding properties. For example, 1*T*-phase zirconium and hafnium dichalcogenides are considered for photovoltaic applications due to their suitable band gap for visible light absorption [18,19]. Moreover, the monolayer TMDs with CdI_2 type structure are expected to realize low lattice thermal conductivity and enhanced figure of merit (Z_T) due to the strong hybridization of low-lying optical modes with acoustic modes [20–22].

Spin-orbit coupling (SOC) can induce spin polarization in nonmagnetic three-dimensional (3D) crystals when the inversion symmetry is broken, as manifested by the bulk Rashba-type (referred to as R-1) and Dresselhaus-type (referred to as D-1) effects [23,24]. Recently, a new insight indicates that fundamental spin polarization effects can originate from the local asymmetry (atomic site group) rather than the global asymmetry (bulk space group) [25]. Consequently, the doubly degenerate bands due to inversion symmetry and time reversal symmetry in nonmagnetic centrosymmetric materials could have opposite polarization, each spatially localized on one of the two separate sectors forming the inversion partners. In other words, spin-layer locking effect, where spin polarization spatially separated in two real space sectors forming the inversion partners, can be invoked, which introduces type-2 Rashba (R-2) and Dresselhaus (D-2) effects. Compared with the R-1 effect under a large internal electric field, the R-2 effect may have advantages for electrically tunable spintronics devices due to the easy manipulation of spins via the application of an external electric field [26–28].

* Corresponding authors.
E-mail addresses: xrchen@scu.edu.cn (X.-R. Chen), smeng@iphy.ac.cn (S. Meng).

https://doi.org/10.1016/j.scib.2017.12.003
2095-9273/

In experiment, hidden spin-polarized bulk bands in an inversion-symmetric bulk TMDs (for example, bulk WSe_2 [29] and bulk MoS_2 [30]) have been observed. A lot of theoretical works have been reported on hidden spin polarization in centrosymmetric materials [31,32]. Moreover, Bruyer et al. [33] proposed the possibility of combining ferroelectricity and Rashba-like spin splitting in monolayer 1*T*-phase transition-metal dichalcogenides MX_2 (M = Mo, W; X = S, Se, Te). Recently, helical spin texture with spin-layer locking in monolayer $PtSe_2$ has been revealed by combining spin- and angle-resolved photoemission spectroscopic (spin-ARPES) measurements [34]. Such spin physics including a local Rashba effect possesses a great potential for building electric-field-tunable spintronic devices. The investigation of hidden spin polarization in two-dimensional materials with local centrosymmetry opens a new era. Therefore, prediction and realization of hidden spin polarization in layered materials becomes an important research frontier for materials science and quantum physics.

In this work, we present a systematic study on the hidden spin polarization in 1*T*-phase layered TMDs MX_2 (M = Zr, Hf; X = S, Se, Te) based on accurate first-principles calculations. Our results show that spin-layer locking exists in 1*T*-phase monolayer and bilayer MX_2. In particular, the spin-layer locking is most significant for the β-band in valence, which is strongly affected by the strength of spin-orbit coupling and can be easily explored in experiment. The conduction band minimum of ξ-band, located at the high symmetry M point, has a strong anisotropy in helical hidden spin texture. The helical hidden spin texture of bilayer $ZrSe_2$ is preserved if the upmost Se layer is considered as the inversion symmetry partner, while being suppressed with the upper $ZrSe_2$ layer as a whole considered as the inversion symmetry partner. The hidden spin polarization in 1*T*-phase TMDs can be verified by spin-resolved angle-resolved photoemission spectroscopy. This work sheds new light on hidden spin structures to enrich our understanding of spin polarization physics and provides important clues for designing new materials with specific spin texture and spintronic applications.

2. Methods

The optimized geometry and electronic structure of 1*T*-phase MX_2 materials are obtained from first-principles plane wave calculations within density functional theory (DFT) as implemented in the Vienna *ab initio* simulation package (VASP) [35–37]. The projector augmented-wave (PAW) method [38] and Perdew-Burke-Ernzerhof (PEB) exchange-correction functional [39] are used. A cutoff energy of 500 eV for the plane-wave basis set and a Monkhorst-Pack mesh [40] of $12 \times 12 \times 1$ for the Brillouin zone integration are employed for relaxation and $21 \times 21 \times 1$ for self-consistent calculations. Spin-orbit coupling is taken into account to obtain the spin texture. Spin-orbit coupling is calculated by a perturbation $\sum_{i,l,m} V_l^{SO} \vec{L} \cdot \vec{S} |l,m,i\rangle\langle l,m,i|$ to the pseudopotential, where $|l,m,i>$ is the angular momentum eigenstate of the ith atomic site [41]. The spin polarization is evaluated by projecting the calculated wavefunction $|\phi\rangle$ on the spin and orbital basis of each atomic site $C_{i,l,m,\eta}\langle\phi|(s_\eta \otimes |l,m\rangle_{ii}\langle l,m|)|\phi\rangle$ and then summing $C_{i,l,m,\eta}$ for a given spin direction and sector that contains a number of atomic sites in the unit cell. In order to eliminate the spurious interaction between two adjacent monolayers, a vacuum layer larger than 17 Å is adopted in the calculations. All the structures are fully relaxed by using the conjugate gradient method until the maximum Hellmann-Feynman forces acting on each atom is less than 0.01 eV/Å. The phonon dispersion is calculated using density functional perturbation theory [42] as implemented in phonopy code [43].

3. Results and discussion

3.1. Atomic structure of 1T-phase MX_2

Bulk MX_2 (M = Zr, Hf; X = S, Se, Te) has a stable 1*T*-phase layered structure with weak interlayer interactions, corresponding to the CdI_2-type trigonal structure with $P\bar{3}m1$ space group (No. 164, D_{3d}). In each layer, the transition metal M atoms are sandwiched by the top and bottom chalcogen X layers with inversion symmetry, where the M atoms are octahedrally coordinated by the X atoms. The atomic structure of MX_2 is shown in Fig. 1. In monolayer MX_2, the top layer chalcogens X (red dotted rectangle online) and bottom layer chalcogens X (blue dotted rectangle online) are the inversion symmetry partners, which can be distinguished as the upper-sector and down-sector (labeled up- and down-component, respectively). Meanwhile, in the bilayer $ZrSe_2$, either we choose the upmost Se (Se1) and the bottom Se (Se4) layer as inversion symmetry partners, or the upper and bottom $ZrSe_2$ layer to form the complete symmetry partners for the bilayer $ZrSe_2$ (see Fig. 1).

Note that the possible polymorphs in monolayer MX_2 can only be of trigonal (T) or hexagonal (H) symmetry [44]. The lattice constants of 1*T*-phase monolayer Zr-compounds (ZrS_2, $ZrSe_2$, $ZrTe_2$) are calculated to be 3.68, 3.80 and 3.95 Å, respectively. For comparison, the lattice constants of 1*T*-phase monolayer Hf-compounds (HfS_2, $HfSe_2$, $HfTe_2$) are calculated to be 3.64, 3.76 and 3.97 Å, respectively. All these values are obtained on the level of DFT with PBE functional, and are well consistent with previous results [20–22]. The 2*H*-phase of monolayer Zr- and Hf-compounds is dynamically unstable judged from the phonon dispersion relation (see Fig. S1a and b online for monolayer $ZrSe_2$ as an example) and the fact that the energy of 2*H*-phase is several hundred meV higher than that of the corresponding 1*T*-phase (Table S1 online). Therefore, we focus on the dynamically stable, 1*T*-phase of monolayer TMDs as shown in Fig. 1a.

3.2. Electronic structure and spin textures of monolayer $ZrSe_2$

We first investigate the electronic structure of monolayer $ZrSe_2$ as an example. The band structure of monolayer $ZrSe_2$ is shown in Fig. 2a, where the conduction bands (CB) and valence bands (VB) are shown in the upper and lower panel, respectively. It is consistent with experimental band structure measured by ARPES [45]. Note that all the energy bands are doubly degenerate because of the inversion symmetry and time reversal symmetry.

Fig. 2b shows the orbital-projected electronic band structure. The bottom three conduction bands (labeled as **θ**, **η** and ξ in Fig. 2a, respectively) is mainly composed of the 4*d* orbitals of Zr atoms. The conduction band minimum (CBM) is located at the high symmetry M point, which is mainly composed of d_{xz}, d_{z^2} orbitals of Zr atoms and a part of out-plane p_z orbital of Se atoms. Moreover,

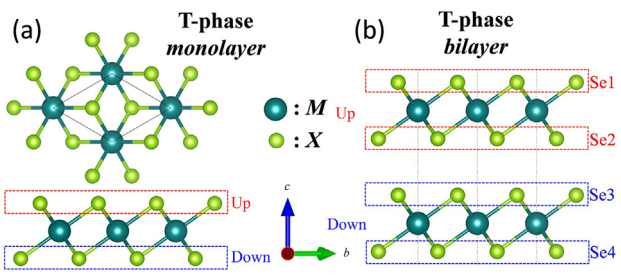

Fig. 1. (Color online) Atomic structure for the 1*T*-phase of layered MX_2 materials. (a) The top and side view of 1*T*-phase MX_2 monolayer. The thin black line denotes the unit cell. (b) Side view of 1*T*-phase (AA-stacking) bilayer MX_2.

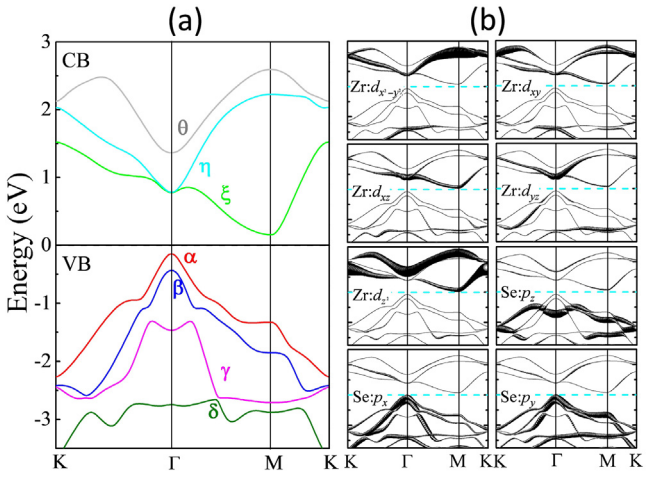

Fig. 2. (Color online) Band structure of monolayer $ZrSe_2$. (a) Band structure of 1*T*-phase monolayer $ZrSe_2$. Three conduction bands (CB) are labeled by **θ**, **η** and **ξ**. Four valence bands (VB) are labeled by **α**, **β**, **γ** and **δ**. (b) The orbital-projected electronic band structure with spectral weight composed by five *d* orbitals of Zr atoms and three *p* orbitals of Se atoms.

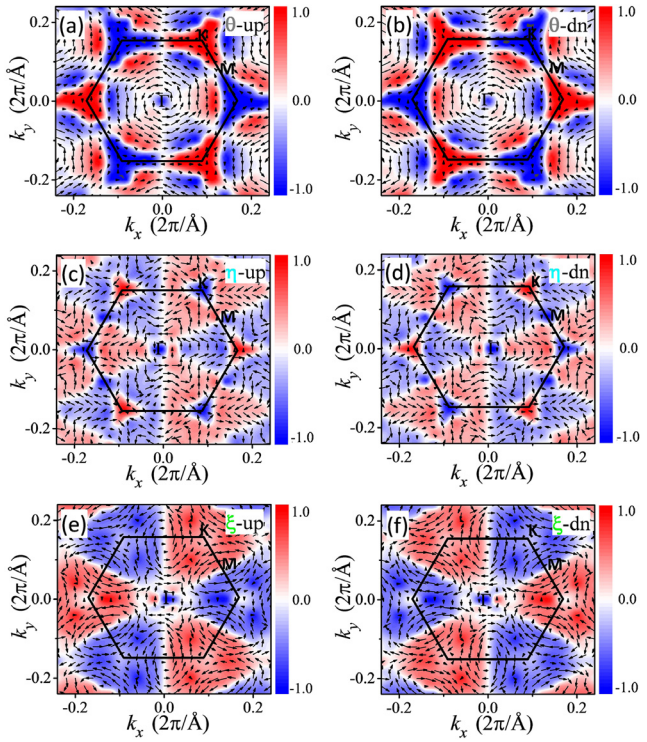

Fig. 3. (Color online) The hidden spin textures for the conduction bands of monolayer $ZrSe_2$. (a) and (b) Spin texture of **θ**-band. (c) and (d) Spin texture of **η**-band. (e) and (f) Spin texture of **ξ**-band (conduction band minimum). Spin texture projected on upper Se atoms and bottom Se atoms, respectively. The color scale quantifies the percentage of out-of-plane spin polarization, S_z. Black arrows demonstrate the orientation of in-plane spin polarization and the length represents the strength of in-plane spin polarization.

the CBM located at the high symmetry M point may be useful to spintronic device because it is convenient for electron excitation, which is better than located at the arbitrary point in the line connecting Γ and M for the iso-structure monolayer $PtSe_2$ [34]. The top four valence bands are labeled as **α**, **β**, **γ** and **δ** band, respectively, according to the ordering in their relative energy. The **α**-band and **β**-band are mainly associated with the in-plane $p_{x,y}$ orbitals of Se atoms. When the spin-orbit coupling is included, the degenerated **α**- and **β**-band opens a gap with 280 meV at the Γ point. The **γ**-band is mainly composed of out-of-plane p_z orbital of Se atoms. And the **δ**-band comes from the significant hybridization of $d_{x^2-y^2}$, d_{xy} orbital of Zr atoms and in-plane $p_{x,y}$ orbital of Se atoms.

The hidden spin texture of conduction bands of monolayer $ZrSe_2$ is shown in Fig. 3. The left panels and right panels show spin polarization projected onto the upper and bottom Se atomic layer, respectively. Note that contour color filling exhibits a C_3 symmetry due to the intrinsic C_{3v} symmetry in the atomic structure of monolayer $ZrSe_2$. Black arrows demonstrate the orientation of in-plane spin polarization, with the orientation angle Θ defined as $\tan\Theta = \frac{S_y}{S_x}$. The length of the black arrows represents the strength of in-plane spin polarization ($S = \sqrt{S_x^2 + S_y^2}$). The color scale quantifies the percentage of out-of-plane spin polarization, S_z.

Fig. 3a and b shows the hidden spin texture for the **θ**-band, where the in-plane spin polarization presents a helical feature mainly located at the vicinity of Γ point in the Brillouin zone. The spin polarization projected onto the upper-sector and down-sector of monolayer $ZrSe_2$ show a counter-clockwise and clockwise helical feature, respectively. Such a helical feature disappears at the vicinity of K and M point. We note that in-plane spin polarization rotating around Γ point shows an isotropic feature, which might attribute to that the d_{z^2} orbital component of Zr atoms is isotropic. For comparison, Fig. 3c and d shows the hidden spin texture for the **η**-band, where the in-plane spin polarization rotates around the Γ and M point. In-plane spin polarization diminishes at K point. Moreover, the spin rotations around Γ and M point are anisotropic, which might come from the hybridization between *d* orbit of Zr atoms and *p* orbit of Se atoms at the Γ and M point. The spin texture of **ξ**-band is shown in Fig. 3e and f. The in-plane spin polarization also shows a helical feature at the Γ point and M point for the **ξ**-band, it shows a large anisotropy around the M point. We infer that such a feature may also come from the same hybridization and the strong anisotropy in band dispersion along M-K and M- Γ directions. From above discussion on the hidden spin texture of conduction bands, we conclude that the helical spin texture and its strong anisotropy at the conduction band minimum of the **ξ**-band (M point) may be useful for practical spintronic device applications. However, we also note that for monolayer $ZrSe_2$ the two inversion-partner sectors are Se layers, while the bottom three conduction bands are mainly composed of the 4*d* orbitals of Zr atoms. It is thus interesting to discuss the effect of Se layers on the Zr bands, the **ξ**-band at M point comprises a different fraction of p_x, p_y, and p_z orbitals of Se atoms, which results an unequal mixing of d_{xz} and d_{yz} orbitals of Zr atoms for the same band at M. A detailed analysis on such effects is subject to further studies in the future.

The hidden spin textures for the valence bands of monolayer $ZrSe_2$ are shown in Fig. 4. Common features on the hidden spin texture are similar to those for the conduction bands in Fig. 3. Here, we mainly focus on the spin structure at the vicinity of Γ point. More details on spin textures for the full Brillouin Zone (BZ) are shown in Fig. S2 (online). For the **α**-band, we can clearly see that the in-plane spin polarization almost disappears around the Γ point. Meanwhile, the out-of-plane spin polarization shows a large value at the vicinity of Γ point. For the **β**-band, the in-plane spin texture shows a large value and rotates around the vicinity of Γ point. The counter-clockwise and clockwise spin textures localized at the top and bottom Se layer correspond to the up- and down-sector of the inversion symmetry in the $ZrSe_2$ monolayer, respectively. It is surprising that the out-of-plane spin polarization (S_z) is almost zero around the Γ point, which is radically different from the features for the **α**-band. Comparing the spin texture between **α**-band and **β**-band near the Fermi level, it is convenient to switch

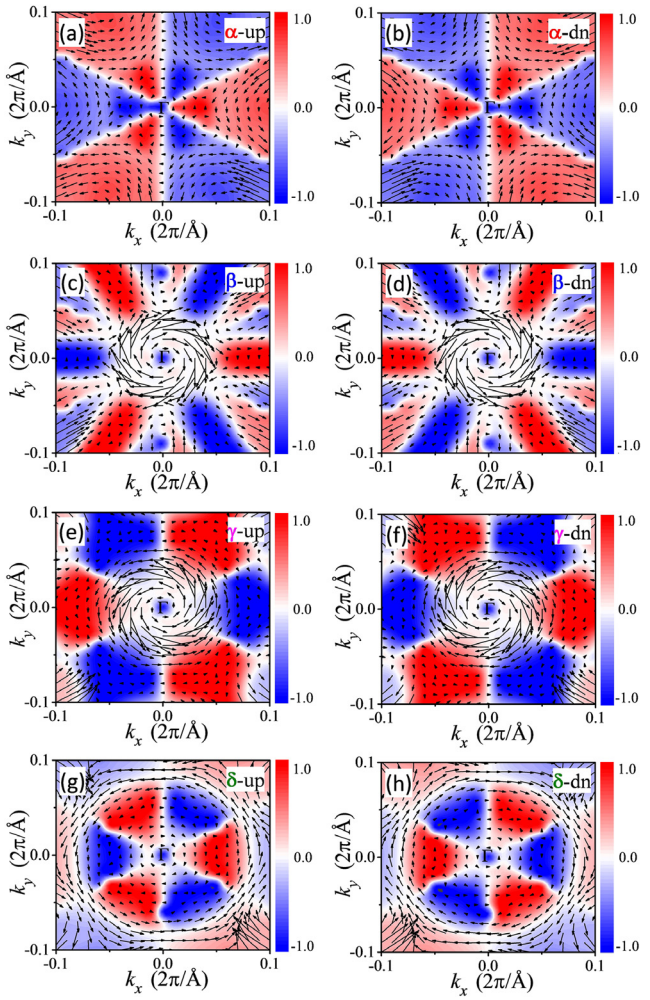

Fig. 4. (Color online) The hidden spin textures of valence band of monolayer $ZrSe_2$. (a) and (b) Spin texture of **α**-band. (c) and (d) Spin texture of **β**-band. (e) and (f) Spin texture of **γ**-band. (g) and (h) Spin texture of **δ**-band. Spin texture projected on upper Se atoms and bottom Se atoms, respectively.

the in-plane and out-of-plane spin polarization by controlling the value of Fermi level. The out-of-plane spin component can also be used in spintronic devices for switching between spin up and down component under an external field. We further note that the direction of spin rotation around Γ point is the same as that at the vicinity of K point (Fig. S2 online). For comparison, in distorted monolayer t-MoS_2 the direction of Rashba-like spin texture around Γ point is reversed as that at the vicinity of K point [33]. The hidden spin texture of **γ**-band is shown in Fig. 4e and f, where the direction of spin rotation is reversed to that for the **β**-band, besides that the energy location is lower and the value of out-of-plane spin polarization (S_z) is smaller. For **δ**-band, the in-plane spin texture is almost zero at a large area around Γ point. It would be useless for spintronic applications because the in-plane spin component approximated to zero and located at very low energy.

From above discussion on the hidden spin polarization of the valence bands, one may ask why the β-band shows the most prominent helical spin texture and spin-layer locking effect. In fact, based on the analysis of spin-orbit coupling (SOC), we find that the spin components of **α**-band and **β**-band, mainly composed of the bonding states of Se $p_{x,y}$ orbitals, have a total z-direction angular momentum $\pm\frac{3}{2}$ and $\pm\frac{1}{2}$, respectively. Therefore, the projected spin component ($S_{x,y}$) of **α**-band vanishes at a small momentum around Γ point, while the **β**-band shows a large value. The helical hidden spin texture of **β**-band is more useful for practical spintronic device applications, since **β**-band has the largest in-plane spin component sensitive to ARPES probe. Recently, the hidden spin texture indeed has been observed by ARPES experiments for the iso-structure $PtSe_2$ monolayer semiconductor films [34].

3.3. Electronic structure and spin textures of bilayer $ZrSe_2$

We now turn to the hidden spin texture for the bilayer $ZrSe_2$. Considering AA-stacking is the energetically favorable vertical stacking pattern for bilayer MX_2, we have studied the electronic structures of the bilayers Zr- and Hf-compounds possessing AA-stacking in the trigonal (T) phase. For completeness, AB-stacking in the hexagonal (H) phase is also considered. Table S1 (online) lists the structural parameters for the equilibrium configuration of layered MX_2. The 2H-phases of bilayer Zr-compounds and Hf-compounds are dynamically unstable from the phonon dispersion calculations (see Fig. S1c and d (online) for bilayer $ZrSe_2$ as an example) and the energies of 2H-phase are several hundred meV higher than the corresponding 1T-phase (Table S1 online). Moreover, the distance d (defined as vertical distance of metal atoms, unit: Å) of 1T-phase about 0.4 Å lower than 2H-phase is shown in Table S1 (online). Therefore, we mainly focus on the 1T-phase of bilayer TMDs as shown in Fig. 1b.

Fig. 5 shows the band structure of bilayer $ZrSe_2$. Each $ZrSe_2$ monolayer has the inversion symmetry, which is different from the 2H-phase monolayer MoS_2 [17]. The bottom four conduction bands are labeled as η_1, η_2, ξ_1 and ξ_2-band. The conduction band minimum (CBM) is also located at the high symmetry point M. The top four valence bands are labeled by α_1, α_2, β_1 and β_2, respectively, convenient for comparison with the labels in the band structure of monolayer $ZrSe_2$ (Fig. 2a). In fact, the pairs of α_1-band and β_1-band are not coming from the contribution of the same monolayer. The α_2-band and β_2-band are either not coming from the contribution of the other layer. All the bands are equally contributed by the two layers of $ZrSe_2$ in the bilayer system.

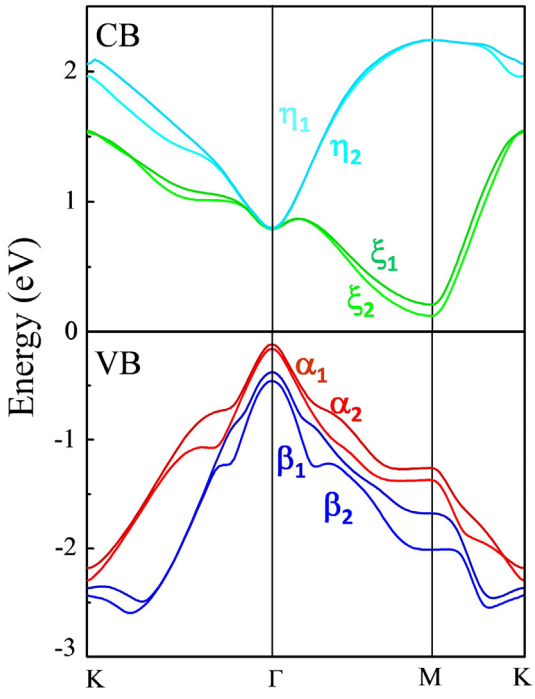

Fig. 5. (Color online) Band structure of 1T-phase $ZrSe_2$ bilayer. Four conduction bands are labeled by η_1, η_2, ξ_1 and ξ_2. Four valence bands are labeled by α_1, α_2, β_1, β_2.

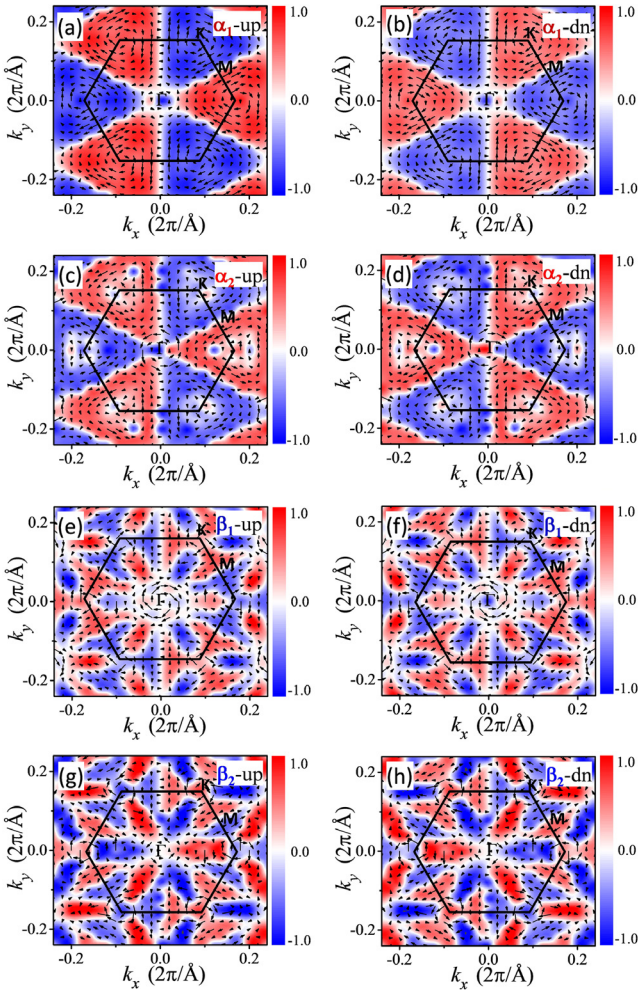

Fig. 6. (Color online) Spin textures projected on upmost Se layer ("up") and bottom Se layer ("down") in the bilayer $ZrSe_2$. (a) and (b) Spin texture of $\boldsymbol{\alpha_1}$-band. (c) and (d) Spin texture of $\boldsymbol{\alpha_2}$-band. (e) and (f) Spin texture of the $\boldsymbol{\beta_1}$-band. (g) and (h) Spin texture of the $\boldsymbol{\beta_2}$-band.

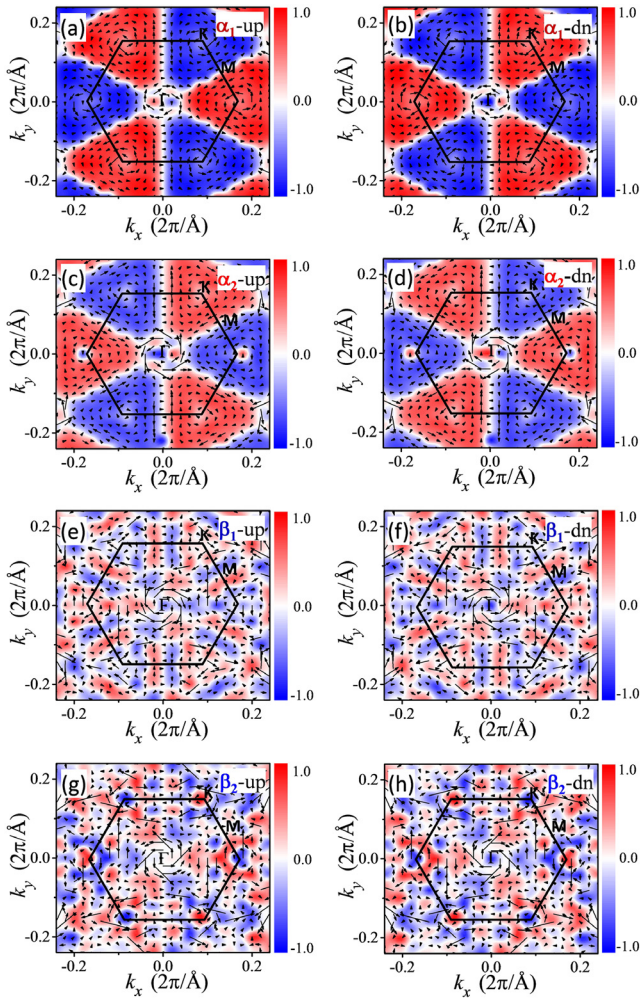

Fig. 7. (Color online) Spin textures projected on upper $ZrSe_2$ layer ("up") and bottom $ZrSe_2$ layer ("down") as inversion partners in the bilayer $ZrSe_2$. (a) and (b) Spin texture of $\boldsymbol{\alpha_1}$-band. (c) and (d) Spin texture of $\boldsymbol{\alpha_2}$-band. (e) and (f) Spin texture of the $\boldsymbol{\beta_1}$-band. (g) and (h) Spin texture of the $\boldsymbol{\beta_2}$-band.

Depending on the definition of inversion symmetry partners in the bilayer $ZrSe_2$, the spin texture localized on the upmost Se atomic layer and that localized on the upper bilayer $ZrSe_2$ layer ars shown in Figs. 6 and 7, respectively. For the former, the upmost Se (Se1) and the bottom Se (Se4) layer are defined as inversion symmetry partners. While the upper and bottom $ZrSe_2$ layer can also be used as inversion symmetry partners to form the complete 2D crystal (see Fig. 1). From Fig. 6, we find that the hidden spin textures localized on the upmost and bottom Se layer resemble those for the single Se layer in the $ZrSe_2$ monolayer case, which is reasonable (Compare Figs. 6 and S2). Moreover, spin textures projected on Se2 and Se3 layers are also shown in Fig. S3. We find that for α bands spin textures on Se1 and Se2 are similar to each other, and spin textures on Se3 and Se4 are almost identical. For the β bands, spin textures localized on Se2 layer resembles those on Se4 (except the $\boldsymbol{\beta_1}$ and $\boldsymbol{\beta_2}$ band are switched), and spin textures localized on Se3 layer resembles those on Se1 (except the $\boldsymbol{\beta_1}$ and $\boldsymbol{\beta_2}$ band are switched). Putting all these data together, it is clear that the Se1 and Se4 layer form a pair of inversion partners. We note that the bilayer $ZrSe_2$ shows the feature of spin-layer locking, similar to the layer-resolved and momentum-dependent spin polarization in 2*H*-phase superconductor $NbSe_2$ [46].

On the other hand, Fig. 7a–d show the hidden spin texture of $\boldsymbol{\alpha_1}$, $\boldsymbol{\alpha_2}$-band localized at the upper and bottom $ZrSe_2$ layer as the up and down sector of the inversion symmetry partners. We find that the rotation spin texture at the vicinity of Γ point is reversed, comparing with that at the vicinity of K point, which is different from the case for monolayer $ZrSe_2$. We find that the total spin polarization of the upper and bottom $ZrSe_2$ layer is approximately zero. Therefore, upon this definition of inversion symmetry partners, the helical hidden spin texture of bilayer MX_2 is suppressed because of the opposite spin polarization contributed by the two almost-degenerate bands $\boldsymbol{\alpha_1}$ and $\boldsymbol{\alpha_2}$. Fig.7e–h display the hidden spin textures of $\boldsymbol{\beta_1}$, $\boldsymbol{\beta_2}$-band, which show similar features as those for $\boldsymbol{\alpha_1}$, $\boldsymbol{\alpha_2}$-band. From the contour color scales plotted in Fig. 7, we find that the spin component along *z* direction of the $\boldsymbol{\beta_1}$, $\boldsymbol{\beta_2}$-band is smaller than that for $\boldsymbol{\alpha_1}$, $\boldsymbol{\alpha_2}$-band. Similar to the monolayer case, it is also the result of total *z*-direction angular momentum being $\pm\frac{3}{2}$ and $\pm\frac{1}{2}$ for $\boldsymbol{\alpha}$ and $\boldsymbol{\beta}$ bands, respectively.

3.4. Hidden spin polarization in other MX_2

To explore whether the hidden spin features are generic among the MX_2 materials studied here, Fig. 8 shows the valence band structure for monolayer Zr- and Hf-compounds. The conduction band of monolayer Zr-compounds and Hf-compounds are shown in Fig. S4 (Supplementary data). We find that the overall band

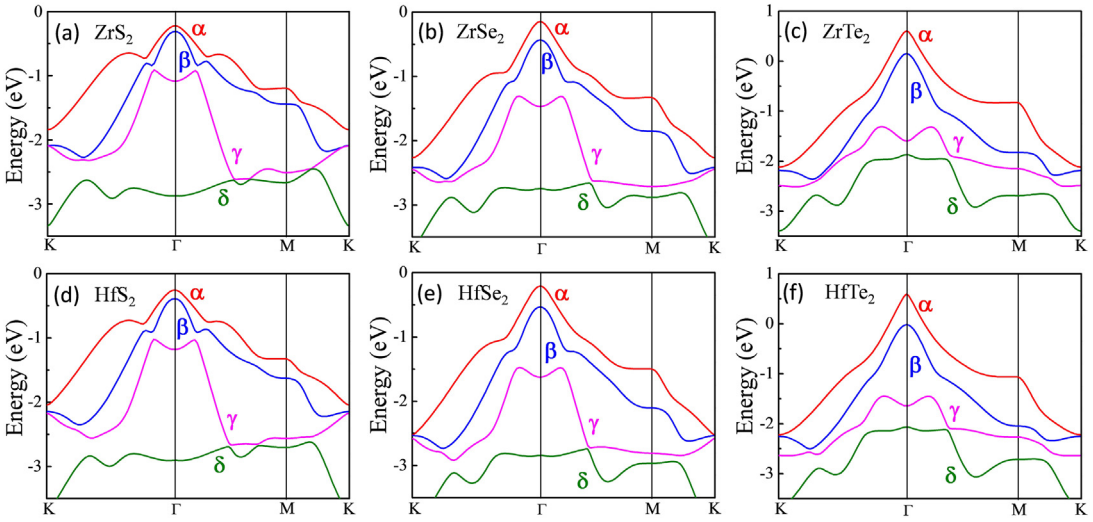

Fig. 8. (Color online) The band structure of valence bands of MX_2 monolayer. (a)–(c) The valence bands of monolayer Zr-compounds. (d)–(f) The valence bands of monolayer Hf-compounds. Four valence bands are labeled by **α**, **β**, **γ** and **δ** in all cases.

structures are very similar to that for $ZrSe_2$. It is worth noting that monolayer $ZrTe_2$ and $HfTe_2$ are metallic, which is difficult to have spin textures conserved in experimental measurement. More details about the structures of these compounds can be found in Table S1.

From all above analyses, the **β**-band is very close to the Fermi energy and can be easily measured experimentally, which is justified by the recent experiments on the iso-structure of monolayer $PtSe_2$ films [34]. Figs. 9 and 10 show the spin texture of **β**-band for monolayer Zr- and Hf-compounds, respectively. In addition, the spin textures of conduction band minimum of Zr-compounds and Hf-compounds are shown in Figs. S5 and S6, respectively. By comparing the Zr- and Hf-compounds, we find that the strength of in-plane spin polarization of heavy element Hf is larger than Zr counterpart. We conclude that the strength of spin-orbit coupling strongly affects the value of spin polarization. By comparing the influence of the S, Se, and Te atoms on the spin texture structures, we find that the in-plane spin component increases with the increasing of elemental radius (for example, Te atom is larger than S atom), which also comes from the stronger spin-orbital interactions in heavier chalcogens. Again, we expect that high-quality $HfSe_2$ films could be suitable candidates for verifying above theoretical predictions by experimental measurement, because of its semiconductor nature and strong spin-orbit coupling effects with heavy atoms.

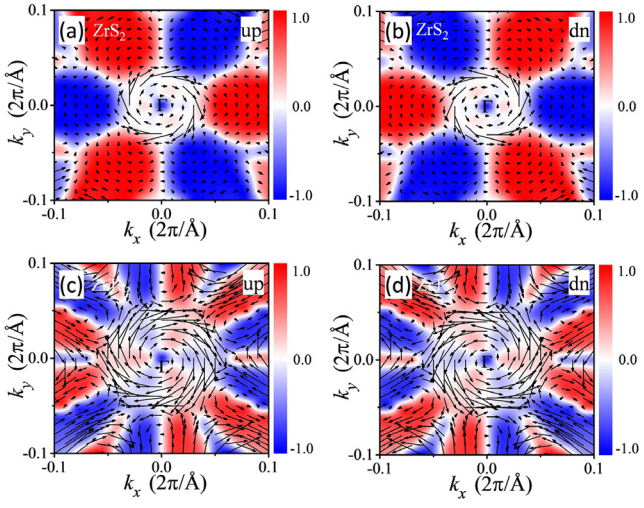

Fig. 9. (Color online) The hidden spin textures of β-band for Zr-compounds. (a) and (b) The spin texture of 1*T*-phase monolayer ZrS_2. (c) and (d) The spin texture of 1*T*-phase monolayer $ZrTe_2$.

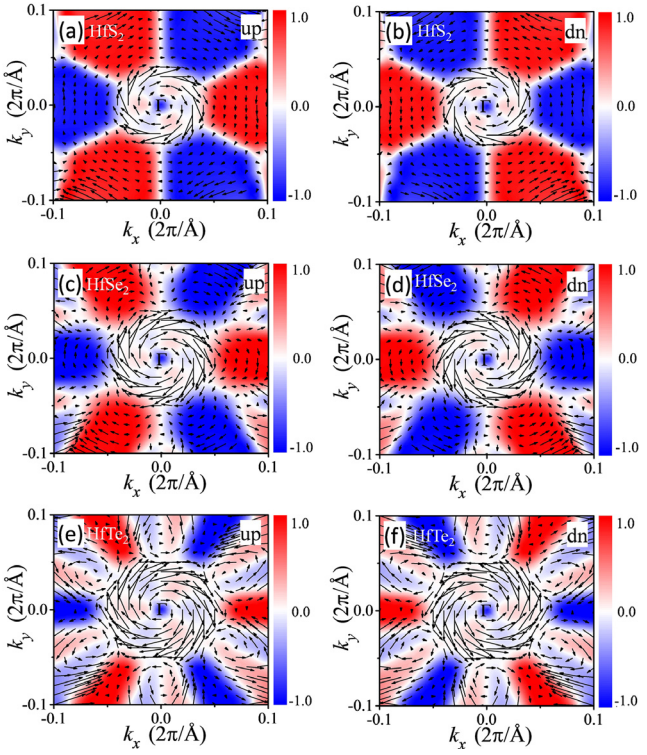

Fig. 10. (Color online) The hidden spin textures of β band for Hf-compounds. (a) and (b) The spin texture of 1*T*-phase monolayer HfS_2. (c) and (d) The spin texture of 1*T*-phase $HfSe_2$ monolayer. (e) and (f) The spin texture of 1*T*-phase $HfTe_2$ monolayer.

4. Conclusion

First-principles calculations are performed to investigate the hidden spin polarization in 1*T*-phase layered transition-metal dichalcogenides MX_2 (M = Zr, Hf; X = S, Se, Te). Strong spin-layer locking effect has been found, namely, energy-degenerate opposite

spins spatially separated in the top and bottom layer, respectively. Furthermore, the spin texture of β-band can be easily probed, which is strongly affected by the strength of spin-orbit coupling of transition metal and chalcogen elements. The conduction band minimum of ξ-band in high symmetry M point has a strong anisotropy in helical hidden spin texture. Hidden spin polarization in 1*T*-phase TMDs predicted here can be observed by spin-resolved and angle-resolved photoemission spectroscopy experiments in the future. This work provides an important clue to search for specific spin textures in two dimensional materials and enriches our understanding of spin polarization physics.

Conflict of interest

The authors declare that they have no conflict of interest.

Acknowledgments

This work was financially supported by the National Basic Research Program of China (2015CB921001, 2013CBA01600, and 2016YFA0300902), the National Natural Science Foundation of China (61306114), "Strategic Priority Research Program (B)" of Chinese Academy of Sciences (XDB07030100), the National Natural Science Foundation of China Academy of Engineering Physics (U1430117), and the Science Challenge Project (TZ2016001). We also acknowledge the computing resources from Tianjin Supercomputing Center.

Appendix A. Supplementary data

Supplementary data associated with this article can be found, in the online version, at https://doi.org/10.1016/j.scib.2017.12.003.

References

[1] Morosan E, Zandbergen HW, Dennis BS, et al. Superconductivity in Cu_xTiSe_2. Nat Phys 2006;2:544–50.
[2] Ye JT, Zhang YJ, Akashi R, et al. Superconducting dome in a gate-tuned band insulator. Science 2012;338:1193–6.
[3] Radisavljevic B, Radenovic A, Brivio J, et al. Single-layer MoS_2 transistors. Nat Nanotechnol 2011;6:147–50.
[4] Yin Z, Li H, Li H, et al. Single-layer MoS_2 phototransistors. ACS Nano 2012;6:74–80.
[5] Xiao D, Liu GB, Feng W, et al. Coupled spin and valley physics in monolayers of MoS_2 and other group-VI dichalcogenides. Phys Rev Lett 2012;108:196802.
[6] Zeng H, Dai J, Yao W, et al. Valley polarization in MoS_2 monolayers by optical pumping. Nat Nanotechnol 2012;7:490–3.
[7] Mak KF, He K, Shan J, et al. Control of valley polarization in monolayer MoS_2 by optical helicity. Nat Nanotechnol 2012;7:494–8.
[8] Liu J, Hou WJ, Cheng C, et al. Intrinsic valley polarization of magnetic VSe_2 monolayers. J Phys Condens Matter 2017;29:255501.
[9] Shirodkar SN, Waghmare UV. Emergence of ferroelectricity at a metal-semiconductor transition in a 1*T* monolayer of MoS_2. Phys Rev Lett 2014;112:157601.
[10] Hsu YT, Vaezi A, Fischer MH, et al. Topological superconductivity in monolayer transition metal dichalcogenides. Nat Commun 2017;8:14985.
[11] Wang Y, Li L, Yao W, et al. Monolayer $PtSe_2$, a new semiconducting transition-metal-dichalcogenide, epitaxially grown by direct selenization of Pt. Nano Lett 2015;15:4013–8.
[12] Mak KF, Lee C, Hone J, et al. Atomically thin MoS_2: a new direct-gap semiconductor. Phys Rev Lett 2010;105:136805.
[13] Nan H, Wang Z, Wang W, et al. Strong photoluminescence enhancement of MoS_2 through defect engineering and oxygen bonding. ACS Nano 2014;8:5738–45.
[14] Song Y, Wang X, Mi WB. Spin splitting and reemergence of charge compensation in monolayer WTe_2 by 3*d* transition-metal adsorption. Phys Chem Chem Phys 2017;19:7721–7.
[15] Cheng YC, Zhu ZY, Mi WB, et al. Prediction of two-dimensional diluted magnetic semiconductors: doped monolayer MoS_2. Phys Rev B 2013;87:100401.
[16] Feng N, Mi WB, Cheng YC, et al. First principles prediction of the magnetic properties of Fe-X_6 (X = S, C, N, O, F) doped monolayer Mo_S2. Sci Rep 2014;4:3987.
[17] Cheng C, Sun JT, Chen XR, et al. Nonlinear Rashba spin splitting in transition metal dichalcogenide monolayers. Nanoscale 2016;8:17854–60.
[18] Lebegue S, Bjorkman T, Klintenberg M, et al. Two-dimensional materials from data filtering and Ab initio calculations. Phys Rev X 2013;3:031002.
[19] Jiang H. Structural and electronic properties of ZrX_2 and HfX_2 (X = S and Se) from first principles calculations. J Chem Phys 2011;134:204705.
[20] Gu X, Yang R. Phonon transport in single-layer transition metal dichalcogenides: a first-principles study. Appl Phys Lett 2014;105:131903.
[21] Yumnam G, Pandey T, Singh AK. High temperature thermoelectric properties of Zr and Hf based transition metal dichalcogenides: a first principles study. J Chem Phys 2015;143:234704.
[22] Ding G, Gao GY, Huang Z, et al. Thermoelectric properties of monolayer MSe_2 (M = Zr, Hf): low lattice thermal conductivity and a promising figure of merit. Nanotechnology 2016;27:375703.
[23] Dresselhaus G. Spin-orbit coupling effects in zinc blende structures. Phys Rev 1955;100:580.
[24] Rashba EI. Properties of semiconductors with an extremum loop. 1. Cyclotron and combinational resonance in a magnetic field perpendicular to the plane of the loop. Sov Phys Solid State 1960;2:1109.
[25] Zhang X, Liu Q, Luo JW, et al. Hidden spin polarization in inversion-symmetric bulk crystals. Nat Phys 2014;10:387.
[26] Liu Q, Guo Y, Freeman AJ. Tunable rashba effect in two-dimensional $LaOBiS_2$ films: ultrathin candidates for spin field effect transistors. Nano Lett 2013;13:5264–70.
[27] Liu Q, Zhang X, Jin H, et al. Search and design of nonmagnetic centrosymmetric layered crystals with large local spin polarization. Phys Rev B 2015;91:235204.
[28] Kepenekian M, Robles R, Katan C, et al. Rashba and dresselhaus effects in hybrid organic inorganic perovskites: from basics to devices. ACS Nano 2015;9:11557–67.
[29] Riley JM, Mazzola F, Dendzik M, et al. Direct observation of spin-polarized bulk bands in an inversion-symmetric semiconductor. Nat Phys 2014;10:835.
[30] Razzoli E, Jaouen T, Mottas ML, et al. Selective probing of hidden spin-polarized states in inversion-symmetric bulk MoS_2. Phys Rev Lett 2017;118:086402.
[31] Zhang H, Liu CX, Zhang SC. Spin-orbital texture in topological insulators. Phys Rev Lett 2013;111:066801.
[32] Sławinska J, Narayan A, Picozzi S. Hidden spin polarization in nonmagnetic centrosymmetric $BaNiS_2$ crystal: signatures from first principles. Phys Rev B 2016;94:24114.
[33] Bruyer E, Sante DD, Barone P, et al. Possibility of combining ferroelectricity and Rashba-like spin splitting in monolayers of the 1*T*-type transition-metal dichalcogenides MX_2 (M = Mo, W; *X* = S, Se, Te). Phys Rev B 2016;94:195402.
[34] Yao W, Wang E, Huang H, et al. Direct observation of spin-layer locking by local Rashba effect in monolayer semiconducting $PtSe_2$ film. Nat Commun 2017;8:14216.
[35] Kresse G, Hafner J. Ab *initio* molecular dynamics for liquid metals. Phys Rev B 1993;47:558–61.
[36] Kresse G, Hafner J. Ab initio molecular-dynamics simulation of the liquid-metal–amorphous-semiconductor transition in germanium. Phys Rev B 1994;49:14251–69.
[37] Kress G, Furthmüller J. Efficient iterative schemes for ab initio total-energy calculations using a plane-wave basis set. Phys Rev B 1996;54:11169–86.
[38] Blochl PE. Projector augmented-wave method. Phys Rev B 1994;50:17953–79.
[39] Perdew JP, Burke K, Ernzerhof M. Generalized gradient approximation made simple. Phys Rev Lett 1996;77:3865–8.
[40] Monkhorst HJ, Pack JD. Special points for Brillouin-zone integrations. Phys Rev B 1976;13:5188–92.
[41] Błonski P, Hafner J. Magnetic anisotropy of transition-metal dimers: density functional calculations. Phys Rev B 2009;79:224418.
[42] Baroni S, Gironcoli S, Corso AD, et al. Phonons and related crystal properties from density-functional perturbation theory. Rev Mod Phys 2001;73:515.
[43] Togo A, Tanaka I. First principles phonon calculations in materials science. Scr Mater 2015;108:1–5.
[44] Wang QH, Zadeh KK, Kis A, et al. Electronics and optoelectronics of two-dimensional transition metal dichalcogenides. Nat Nanotechnol 2012;7:699–712.
[45] Moustafa M, Paulheim A, Mohamed M, et al. Angle-resolved photoemission studies of the valence bands of ZrS_xSe_{2-x}. Appl Surf Sci 2016;366:397–403.
[46] Bawden L, Cooil SP, Mazzola F, et al. Spin–valley locking in the normal state of a transition-metal dichalcogenide superconductor. Nat Commun 2016;7:11711.